

Nanoscale inhibition of polymorphic and ambidextrous IAPP amyloid aggregation with small molecules

Aleksandr Kakinen¹, Jozef Adamcik², Bo Wang³, Xinwei Ge³, Raffaele Mezzenga² (✉), Thomas P. Davis^{1,4} (✉), Feng Ding³ (✉), and Pu Chun Ke¹ (✉)

Nano Res., **Just Accepted Manuscript** • <https://doi.org/10.1007/s12274-017-1930-7>
<http://www.thenanoresearch.com> on Nov. 23, 2017

© Tsinghua University Press 2017

Just Accepted

This is a “Just Accepted” manuscript, which has been examined by the peer-review process and has been accepted for publication. A “Just Accepted” manuscript is published online shortly after its acceptance, which is prior to technical editing and formatting and author proofing. Tsinghua University Press (TUP) provides “Just Accepted” as an optional and free service which allows authors to make their results available to the research community as soon as possible after acceptance. After a manuscript has been technically edited and formatted, it will be removed from the “Just Accepted” Web site and published as an ASAP article. Please note that technical editing may introduce minor changes to the manuscript text and/or graphics which may affect the content, and all legal disclaimers that apply to the journal pertain. In no event shall TUP be held responsible for errors or consequences arising from the use of any information contained in these “Just Accepted” manuscripts. To cite this manuscript please use its Digital Object Identifier (DOI®), which is identical for all formats of publication.

TABLE OF CONTENTS (TOC)

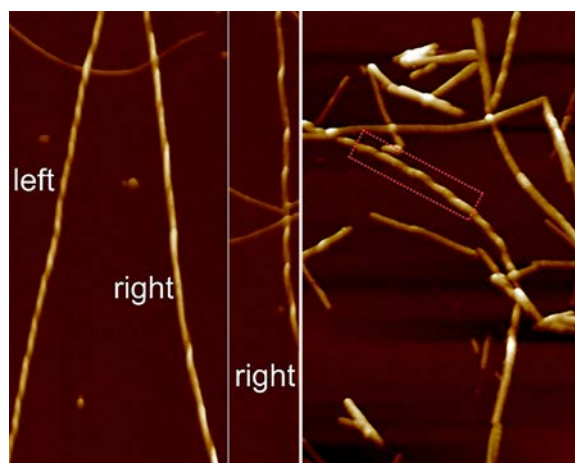
Aleksandr Kakinen,¹ Jozef Adamcik,² Bo Wang,³
Xinwei Ge,³ Raffaele Mezzenga,^{2*} Thomas P. Davis,^{1,4*}
Feng Ding,^{3*} and Pu Chun Ke^{1*}

¹ ARC Centre of Excellence in Convergent Bio-Nano Science and Technology, Monash Institute of Pharmaceutical Sciences, Monash University, 381 Royal Parade, Parkville, VIC 3052, Australia

² Food & Soft Materials, Department of Health Science & Technology, ETH Zurich, Schmelzbergstrasse 9, LFO, E23, 8092 Zurich, Switzerland

³ Department of Physics and Astronomy, Clemson University, Clemson, SC 29634, USA

⁴ Department of Chemistry, Warwick University, Gibbet Hill, Coventry, CV4 7AL, United Kingdom



Human islet amyloid polypeptide (IAPP) in the fibrillar form is polymorphic and ambidextrous possessing multiple periodicities. Upon interfacing with small molecule EGCG, IAPP fibrils displayed kinks and branching but conserved the twisted morphology.

Nanoscale inhibition of polymorphic and ambidextrous IAPP amyloid aggregation with small molecules

Aleksandr Kakinen,¹ Jozef Adamcik,² Bo Wang,³ Xinwei Ge,³ Raffaele Mezzenga,²(✉) Thomas P. Davis,^{1,4}(✉) Feng Ding,³(✉) and Pu Chun Ke¹(✉)

¹ ARC Centre of Excellence in Convergent Bio-Nano Science and Technology, Monash Institute of Pharmaceutical Sciences, Monash University, 381 Royal Parade, Parkville, VIC 3052, Australia

² Food & Soft Materials, Department of Health Science & Technology, ETH Zurich, Schmelzbergstrasse 9, LFO, E23, 8092 Zurich, Switzerland

³ Department of Physics and Astronomy, Clemson University, Clemson, SC 29634, USA

⁴ Department of Chemistry, Warwick University, Gibbet Hill, Coventry, CV4 7AL, United Kingdom

Received: day month year / Revised: day month year / Accepted: day month year (automatically inserted by the publisher)

© Tsinghua University Press and Springer-Verlag Berlin Heidelberg 2011

ABSTRACT

Understanding how small molecules interface amyloid fibrils on the nanoscale is of importance for developing therapeutic treatment against amyloid-based diseases. Here we show, for the first time, that human islet amyloid polypeptide (IAPP) in the fibrillar form is polymorphic and ambidextrous possessing multiple periodicities. Upon interfacing with small molecule epigallocatechin gallate (EGCG), IAPP aggregation was rendered off pathway assuming the form of soft and disordered clusters, while mature IAPP fibrils displayed kinks and branching but conserved the twisted fibril morphology. These nanoscale phenomena resulted from competitive interactions between EGCG and the IAPP amyloidogenic region, as well as end capping of the fibrils by the small molecule. This information is crucial to delineating IAPP toxicity implicated in type 2 diabetes and developing new inhibitors against amyloidogenesis.

KEYWORDS

IAPP fibrillization, persistence length, inhibition, small molecule, DMD simulations

1. Introduction

Protein misfolding and aggregation, regardless of its culprit origin and sequence, is a ubiquitous phenomenon in neurodegenerative diseases and

Address correspondence to Raffaele Mezzenga, raffaele.mezzenga@hest.ethz.ch; Thomas P. Davis, thomas.p.davis@monash.edu; Feng Ding, fding@clemson.edu; and Pu Chun Ke, pu-chun.ke@monash.edu

type 2 diabetes (T2D), characterized by the formation of a cross- β architecture common to all amyloid fibrils and plaques [1–3]. Naturally occurring small molecules curcumin, resveratrol, epigallocatechin-3-Gallate (EGCG), orcein, 2,8-bis-(2,4-dihydroxy-phenyl)-7-hydroxy-phenoxazin-3-one (O4), as well as synthetic polymers and nanoparticles have shown potency in directing the progression of β -amyloid, α -synuclein, islet amyloid polypeptide (IAPP), prions, or cystatin amyloid towards disordered and amorphous aggregates [4–15]. Modifications of the dihydro thiazolo ring-fused 2-pyridone effectively interrupted curli biogenesis of *Escherichia coli* to prevent biofilm formation [16]. However, the nanoscale properties of amyloid inhibition by small molecules remain unclear, hindering the design of new inhibitors targeting amyloidogenesis.

EGCG possesses a modest water solubility (33.3–100 g/L) and high capability in remodelling amyloid fibrils [17]. EGCG redirected the fibrillogenesis of both β -amyloid and α -synuclein into unstructured, nontoxic off-pathway oligomers [18], and remodelled mature amyloid- β and α -synuclein into smaller, amorphous protein aggregates that were nontoxic. EGCG remodelled IAPP amyloid fibrils but did not fully resolubilize them back to monomers, suggesting IAPP fibrillization and EGCG remodelling were irreversible processes [19]. A mutation study revealed that the interactions of EGCG with the aromatic residues, amino groups and sulfhydryls of

IAPP were non-essential for amyloid inhibition and remodelling, pointing to the roles of hydrogen bonding and hydrophobic interaction between the small molecule and the peptide backbone and side chains, respectively [19]. IAPP amyloid inhibition by

EGCG and its protection of IAPP toxicity have been investigated [20], which suggested on-pathway EGCG trapping of the polypeptide into an early intermediate state prior to IAPP amyloid formation. The role of EGCG autoxidation in the remodelling of amyloid- β 1–40, IAPP_{8–24}, or Sup35N^{MAc7–16} Y → F amyloid fibrils has been examined [21], highlighting the importance of hydrophobic interaction for such interactions. EGCG displayed a reduced capacity in inhibiting IAPP aggregation in the presence of a DPPG lipid monolayer, suggesting the competing role of interfaces with IAPP-small molecular interactions [22].

In the present study, we combined high-resolution transmission electron microscopy (TEM) imaging, atomic force microscopy (AFM) and discrete molecular dynamics (DMD) simulations to extract the nanoscale information of IAPP inhibition and remodelling by fresh, autoxidized and glutathione (GSH)-reduced EGCG. We systematically analyzed the persistence length, contour length (definitions see Figs. 1A and S5) as well as morphology of IAPP and IAPP-EGCG products versus time. We report on the polymorphic and ambidextrous nature of IAPP fibrils and reveal the molecular details of EGCG interacting with soluble IAPP and insoluble IAPP fibrils using DMD simulations, a rapid sampling technique for depicting large systems with atomic information. The nanoscale information uncovered by this study has filled a knowledge gap between atomic and cellular level understanding of IAPP

amyloidogenesis and mitigation against type 2 diabetes.

2. Results and discussion

2.1 IAPP interfacing EGCG on the nanoscale

TEM imaging revealed IAPP fibrillization in the presence of EGCG and its derivatives. The representative images for 20 min of incubation are shown in Fig. S-1 in the Electronic Supplementary Material (ESM), which were not analyzed due to the small sizes of IAPP and IAPP-EGCG protofibrils. The selections of 1 h, 6 h and 24 h of fibrillization intended to cover the nucleation, end of elongation and saturation (Fig. 1B) phase, respectively.

IAPP seeds and protofibrils (30~200 nm) emerged after 1 h for IAPP alone and IAPP with fresh, oxidized and GSH-reduced EGCG. In the presence of EGCG, the protofibrils appeared amorphous with multiple splitting branches (Figs. 1f,i,l), differing from the linear contours of the IAPP control (Fig. 1c). After 6 h IAPP formed long fibrils (Fig. 1d) with a broad length distribution (160~17,400 nm) (Fig. 2a), whereas EGCG yielded short and ramified fibrils (Figs. 1g,j,m&2b-d). Fibrillization inhibition was achieved with fresh EGCG at 6 h (contour length: 65~330 nm) (Figs. 1g&2b), whereas oxidized EGCG rendered longer fibrils (40~1,125 nm) (Figs. 1j&2c). At 24 h the IAPP length distribution was further broadened (60~20,600 nm) (Fig. 2a), and all samples displayed polymorphism of long fibrils alongside short, soft and curvy fibrils/protofibrils. Such heterogeneity of IAPP fibrils was also observed by vandenAkker et al. using tip-enhanced Raman spectroscopy [23], where unordered or α helical surface structures contrasted the β -sheet rich fibril core. Coexistence of amyloid and non-amyloid fibrils have been reported for other classes of proteins *in vitro* [24]. Further analysis revealed that long IAPP fibrils were 7.9 (\pm 0.9) nm in thickness, whereas the short ones were 9.8 (\pm 2.5) nm in thickness with more

pronounced variations from their amorphous nature (Fig. 1e inset). In addition, short fibrils re-emerged at 24 h (Fig. 2a, yellow circle), departing from the log-normal distribution for such aggregation process [25,26] and corroborating the possibility of multiple fibrillating rates for IAPP. No small fibrils were observed after one month (Fig. 3f).

Fresh, autoxidized and GSH-reduced EGCG inhibited IAPP fibrillization up to 6 h (Figs. 1b,c-n, 2b-d). Small fibrils were observed at 24 h for all three cases (Figs. 2b-d, grey circles). **It has been shown in literature [20] that EGCG could inhibit IAPP fibrillization up to 200 h, under different buffer conditions and IAPP/EGCG molar ratios. In the present study, fresh EGCG exerted stronger inhibition than oxidized EGCG up to 6 h. At 24 h, both fresh and oxidized EGCG displayed similar length distributions while GSH-reduced EGCG inhibited IAPP fibrillization more effectively. This is likely due to the gradual oxidation of "fresh" EGCG as indicated by its colour change after 6 h, and at 24 h the initially fresh and autoxidized EGCG elicited similar inhibition. With GSH-reduced EGCG shorter and fewer IAPP fibrils were observed than with other EGCG species. FiberApp [27] analysis confirmed a narrower length distribution in the case of GSH-reduced EGCG (Fig. 2d). The persistence length (λ) analysis [27,28] performed with FiberApp revealed 3 distinct fibril species with reduced EGCG (Fig. 2e), whereas other samples displayed the formation of 2 different species - long and rigid fibrils and short and soft fibrils or amorphous aggregates. Accordingly, in the presence of the EGCG species and at 24 h, **the beta-sheet content of IAPP was reduced from 39.2% to 34.3%, 35.7% and 32.9% when exposed to fresh, oxidized and reduced EGCG, respectively, while the unordered structure content was enhanced from 37.3% for the IAPP control to 49.7%, 47.3% and 51.7% for the three EGCG species (Fig. 2f, Fig. S-2 in the ESM).****

The fibrils formed after 1 h appeared significantly softer (λ = 50~118 nm) than the long fibrils (λ = 2,020~2,885 nm) formed after 24 h. This difference in rigidity could stem from the ongoing

elongation and self-assembly of proto-filaments/fibrils into amyloid fibrils (Figs. 3a-c) [28,29]. Twisted fibrils with a defined periodicity were observed at 6 h (Fig. 3a). After 24 h many IAPP fibrils possessed a structural morphology of left-handed twisted fibrils typical for amyloids but with different periodicities (Figs. 3b,d,e) indicating morphological polymorphism of IAPP fibrils. For the first time, right-handed IAPP fibrils were detected (Fig. 3c) indicating that IAPP is able to assemble into fibrils with different handedness. The periodicity of IAPP fibrils increased with the height of fibrils (Figs. 3d,e), similarly to beta-lactoglobulin [28], lysozyme [30] or β -amyloid [31], suggesting a linear growth of primary filaments followed by lateral aggregation into mature amyloids.

Increasing the molar ratio of fresh EGCG to IAPP from 1:1 to 5:1 minimized long fibrils while increased curly aggregates after 6 and 24 h (Fig. S-3 in the ESM). The persistence lengths of the curly aggregates were 102 and 123 nm for the two conditions, consistent with that of IAPP exposed to equal molar ratios of fresh, autoxidized and reduced EGCG (Fig. 2e) due to effective aggregation inhibition.

EGCG possessed a remarkable capability in amyloid remodelling. Shortening of 1 month old fibrils was evident after overnight incubation with EGCG (Fig. 3g). However, despite such significant length reductions, the twisted structures of IAPP fibrils remained largely unaltered upon EGCG exposure (Fig. 3g), suggesting that EGCG cleaved off amyloid fibrils but did not alter the latter's morphology. In addition, the average pitch size of the 1 month-old fibrils remained unchanged w/o EGCG, when evaluated by the autocorrelation function (Fig. 3i).

2.2 Molecular details of IAPP interfacing EGCG

Interfacing EGCG with soluble IAPP. We performed all-atom DMD simulations with 1, 2, 4, 6 and 8 IAPP peptides in the presence of EGCG (ligand), where the molecular ratio of EGCG to IAPP was kept at 1:1 and same peptide concentration was maintained. In

all simulations, we observed binding of EGCG with IAPP (Fig. 4, Fig. S-4 in the ESM). EGCG bound to each other or the peptide, while the peptides continued to grow in the number of contacts (Fig. 4c). The peptides and ligands often formed a single cluster (snapshot in Fig. 4a). Examination revealed that EGCG ligands formed small clusters themselves and scattered inside the amorphous aggregates of both the peptides and the ligands (Fig. 4b). In some simulations, inter-peptide beta-sheets were formed (Fig. 4b). The structural properties of these IAPP-EGCG complexes are drastically different from those between IAPP and resveratrol or curcumin [12]. For resveratrol and curcumin, the hydrophobic ligands aggregated into a nanosized core while IAPP peptides bound to the surface by burying their hydrophobic residues and leaving the hydrophilic residues exposed, forming a well-defined "off-pathway" oligomer to subsequently inhibit fibrillization. For EGCG, the small ligand clusters scattered inside the amorphous aggregates might not prevent the continuous growth of the aggregates, but instead interfered with the formation of an elongated fibril and resulted in the formation of curly aggregates (Figs. 1,2). This difference likely originated from the higher solubility of EGCG than resveratrol or curcumin.

Residues R11, F15, H18, F23 and Y37 exerted significantly stronger binding with EGCG than others (Fig. 4d). As EGCG contains multiple benzene rings, the enrichment of aromatic IAPP residues in binding EGCG indicates that π -stacking is the driving force for IAPP-EGCG interfacing. This finding is reminiscent of our study on the off-pathway nanoassemblies of IAPP with curcumin and resveratrol [12], where the aromatic F15, F23 and Y37 residues were most actively engaged in the binding with the small molecules. The strong binding of EGCG with R11 indicates the importance of hydrogen bonding.

Interfacing EGCG with IAPP fibrils. Using the solid-state NMR derived constraints and two corresponding pentamer fibril models [32,33], we constructed larger fibril models with two decamer

protofibril forming a two-layered fibril (Method; Fig. 4e,f for fibril Model 1 and Fig. S-5 in the ESM for Model 2). EGCG tended to bind aromatic residues – F15, F23 and Y37 – for the edge peptides and residues F15 and Y37 for the interior peptides since F23 was buried inside the fibril (e.g., in simulations with the fibril Model 2, EGCG bound the solvent-exposed F23 & Y37 of the interior peptides instead, Fig. S-5 in the ESM). This is consistent with EGCG binding with soluble IAPPs (Fig. 4a-d). The pivotal role of π -stacking in the assembly of tubular structures was established by Reaches and Gazit [34], where β -amyloid diphenylalanine structural motifs readily assembled into discrete, hollow and stiff nanotubes free of branching and curving. Here the binding of EGCG with F23 of the end IAPP which otherwise was buried inside the fibril implies that EGCG binding may inhibit the fibril growth. Moreover, EGCG molecules binding to the fibril ends formed extensive contacts with the peptides (Figs. 4e,g), resulting in partial unfolding of the peptides at the edges but rest of the peptides still forming beta-sheets with the bulk fibril. Since fibrils undergo dynamic breakage and re-assembly [35], remodelling of IAPP fibrils by EGCG is achieved by competitive binding with the amyloidogenic residues at the fibril edges, which were exposed upon thermodynamic breakage. Capping by EGCG prevented re-assembly into longer fibrils, leading to shorter fibrils with preserved twisted morphology.

Interfacing oxidized EGCG with soluble IAPPs and IAPP fibrils. The oxidized EGCG was modelled after Theasinensin A (ThA), a cross-linked EGCG dimer (Fig. 1b) identified as a major product of EGCG auto-oxidation [36]. DMD simulations were performed for 2, 4, and 6 IAPP peptides mixed with ThA at a 2:1 ratio (i.e., a similar mass ratio to the simulations of EGCG and IAPP) and also for the binding of ThAs with the model IAPP fibril at the same molecular ratio. ThA displayed similar binding profiles with IAPP residues in solution or in the fibril, and formed similar co-aggregated complexes with IAPPs as it was the case with EGCG (Fig. S-7). However, compared to EGCG, ThA had a slower binding with soluble IAPP due to its larger

size and slower diffusion rate. Consequently, EGCG tended to bind IAPP first before IAPP self-association (Fig. 4c and Fig. S-4), but in the case of ThA the self-association IAPP took place before their binding with IAPP (Fig. S-7A). The slower binding of ThA with IAPP could have contributed to the reduced capacity of ThA in inhibiting IAPP aggregation, as observed experimentally.

3. Conclusion

IAPP fibrils displayed both left- and right-handed morphologies with different periodicities (Figs. 3a-e), unlike the morphologies reported for other amyloidogenic proteins. Such polymorphic and ambidextrous characteristics of IAPP fibrils were conserved upon interfacing with EGCG (Figs. 3f-i), pointing to the physical nature of the interaction. EGCG appeared more effective at IAPP amyloid inhibition than remodelling, as corroborated by increased distribution of curly aggregates at elevated EGCG-IAPP molar ratios (Fig. S-3 in the ESM). The comparable effects on IAPP fibrillization inhibition and remodelling by fresh, oxidized and reduced EGCG were indicative of the significance of π -stacking, as hydrogen bonding and hydrophobic interactions were altered while the aromatic EGCG moieties conserved across the three cases. In light of the importance of π -stacking in peptide assembly and inhibition and remodelling of fibrillization [12,33], exploiting this mode of interaction by molecular design may hold the key to effective intervention of peptide aggregation.

It is plausible that the mesoscopic properties of fibrils could have direct or indirect consequences on the cellular interactions, circulation and pathology of the fibrils. In addition, the insight gained from this study could prove beneficial not only to research on amyloidogenesis but also on antibacterial by remodelling of functional amyloids [16,37] to break down their communicative network.

4. Methods

4.1 Materials

Human islet amyloid polypeptide (IAPP) (37-residue sequence: KCNTATCATQRLANFLVHSSNFGAILSSTNVGSNTY; disulfide bridge: 2-7; MW: 3,906) was obtained as lyophilized powder from AnaSpec. Epigallocatechin-3-Gallate (EGCG, $\geq 95\%$ pure) and L-glutathione (GSH, $\geq 98\%$) were acquired from Sigma-Aldrich. The IAPP was weighed on a Cubis MSE balance (Sartorius, 0.01 mg resolution), dissolved in water to a concentration of 100 μM (IAPP is known to fibrillate at μM concentrations *in vitro*), and used immediately for TEM sample preparations. Mature amyloids were generated after dissolving IAPP in water for one month. EGCG stock solutions (1 mM) were prepared immediately or 24 h prior to TEM sample preparations to obtain “fresh” or oxidized EGCG, respectively. The fresh EGCG solution was colourless up to 6 h, while the oxidized EGCG solution appeared light yellow. Therefore the nominally fresh EGCG should have been partially auto-oxidized after 6 h. Reduced EGCG was obtained by mixing the polyphenol with GSH (1 mM stock) at a 1:1 molar ratio in water. All solutions were prepared using degassed ultrapure Milli-Q water (18.2 M Ω -cm; Millipore Corporation, USA).

4.2 Thioflavin T assay

IAPP (25 μM final) was mixed with ThT (25 μM final), fresh, oxidized or reduced EGCG (25 μM final). In addition, as a control ThT was mixed with EGCG derivatives without the addition of IAPP. 100 μL of the each sample was added to a 96-well plate (Costar black/clear bottom) and changes in ThT fluorescence (read from bottom) were recorded every 5 min over 24 h at 25 $^{\circ}\text{C}$ using a FlexStation 3 Multi-Mode Microplate Reader (Molecular Devices; excitation: 440 nm, emission: 485 nm).

4.3 Transmission electron microscopy

The effects of EGCG on the formation and morphology of IAPP amyloids were investigated using high-resolution TEM. For that solutions of IAPP and IAPP mixed with fresh EGCG, oxidized EGCG, or EGCG reduced by GSH were incubated

at room temperature. All chemicals in the test were at 50 μM and the molar ratios of IAPP:EGCG species:GSH were kept at 1:1:1. Approximately 4 μL of each sample solution after 20 min, 1 h, 6 h and 24 h of incubation was pipetted onto a glow discharged (15 s) copper grids (100 mesh; ProSciTech), followed by 60 s of adsorption. Excess samples were then drawn off using filter paper and the grids washed twice by Milli-Q water and excess drawn off as described above. The grids were stained with 2% uranyl acetate for 15 s, with excess stain drawn off, and were air-dried. Imaging was performed by a Tecnai G2 F20 transmission electron microscope (FEI, Eindhoven, The Netherlands), operating at a voltage of 200 kV. Images were recorded using a Gatan UltraScan 1000 (2k \times 2k) CCD camera (Gatan, California, USA) and Gatan Microscopy Suite control software.

4.4 IAPP fibrils tracking and physical characterizations

Fibril tracking and analysis were performed with software FiberApp [27] to determine the effects of EGCG species on the mesoscopic parameters of persistence length (λ), contour length (l) and periodicity ($2p$) of IAPP fibrils. The FiberApp open source code was developed based on statistical polymer physics and enables structural analysis at the single molecular level of high-resolution imaging of fiber-like, filamentous, and macromolecular objects [27]. The persistence length λ reflects an intrinsic property of a polymer, denoting its rigidity and is mathematically defined via the bond correlation function (BCF) in 3D or 2D as the length over which angular correlations in the tangential direction decrease by a factor of e . Here the λ values of IAPP fibrils were estimated using the BCF, mean-squared end-to-end distance (MSED) and mean-squared midpoint displacement (MSMD) methods (Figs. S-5a-f) and presented as average values determined by the three methods (Fig. S-6g in the ESM) [27]. The contour length corresponds to the end-to-end length of a polymer along its contour. In this study the periodicity ($2p$, where p is the pitch size) of a twisting fibril was determined by calculating the intensity autocorrelation function,

while the thickness of the fibrils was analyzed by ImageJ (National Institutes of Health). The values of persistence length and contour length were obtained based on statistical analysis of 4,044 fibrils (Table S1).

4.5 Circular dichroism spectroscopy

Circular dichroism (CD) spectroscopy was utilized to provide insights into the effects of EGCG on the secondary structures of IAPP fibrils. For this we mixed IAPP (25 μ M final) with fresh, oxidized or reduced EGCG (25 μ M final) and pre-incubated the samples for 24 h. CD spectra were taken using a Chirascan Plus qCD instrument (Applied Photophysics) at 0 h and 24 h of incubation. The experiments were performed at 25 $^{\circ}$ C, across a wavelength range of 190 – 260 nm.

4.6 Atomic force microscopy

A droplet of 20 μ L of sample solution (50 μ M each for IAPP and EGCG) was deposited and incubated for 2 min on freshly cleaved mica, rinsed with Milli-Q water, and dried with air. Images were collected using a Nanoscope VIII Multimode Scanning Force Microscope (Bruker) operated in tapping mode in air. Images were flattened using the NanoscopeAnalysis 8.15 software, and no further image processing was done. The statistical analysis of fibrils was performed by FiberApp software.

4.7 Discrete molecular dynamics simulations

DMD is a special type of molecular dynamics (MD) algorithm where continuous potentials are approximated by step-wise potential functions. A detailed description of the DMD algorithm can be found elsewhere [38,39]. Briefly, all molecules were represented by the united-atom model with all heavy atoms and polar hydrogen atoms explicitly modelled, and an implicit solvent model was used. The step-wise potential functions were obtained by mimicking the continuous inter-atomic interaction potentials in the molecular mechanics-based force field, the Medusa force field [40]. Following the same physical laws, the dynamics in DMD is equivalent to continuous potential MD at timescales

longer than picoseconds with differences mainly at short timescales within the sub-picosecond range (i.e., the average time step between two consecutive inter-atomic collisions where a potential energy step is encountered). The interatomic interactions included van der Waals, solvation, electrostatic interactions and hydrogen bond. The solvation energy was modelled by the Lazaridis-Karplus implicit solvent model, EEF1 [40-43]. The distance- and angular-dependent hydrogen bond interaction was modelled using a reaction-like algorithm [41]. Screened electrostatic interactions were computed by the Debye-Hückel approximation. A Debye length of 1 nm was used by assuming a water dielectric constant of 80 and a monovalent electrolyte concentration of 0.1 M. The Anderson's thermostat was used to maintain constant temperature [44].

Small molecule ligands like EGCG were modelled in all-atom DMD simulations with the MedusaScore [41], an extension of the Medusa force field [40]. The MedusaScore was parameterized on a large set of small molecule ligands [41] and transferrable to different molecular systems. The predictive power of MedusaScore has been validated in various benchmark studies, including recent CSAR (community structure-activity resource) blind ligand-receptor docking prediction exercises [45,46] where the performance of MedusaScore was among the best approaches in predicting the near-native ligand-binding poses and binding affinities.

We used the same experimental constraints as Tycko et. al. [32,33] to construct the larger fibril model. In model 1, side chains of Gln10, Leu12, Asn14 and Leu16 were located inward to the beta-sheet formed by residues [28-35,37,38]. The side chains of Arg11, Ala13 and Phe15 in the protofibril were buried to form the fibril. In model 2, the residues mentioned above were located in the opposite direction. We used a central peptide form each of the two models shared by the Tycko group and applied translational and two-fold rotational symmetries to reconstruct the larger fibril. Using the same proximity constraints, we performed

DMD simulations to relax the model structure until the system's potential energies reached equilibrium at 300 K. A total of 20 EGCG monomers were used to maintain a 1:1 ratio between EGCG monomers and IAPP monomers in the fibril. IAPP peptides at both ends of the fibril (magenta in Fig. 4e) were expected to be more flexible than those inside the fibril (cyan). To reduce the computational cost for such a large molecular system, we allowed the four terminal IAPPs to move freely. For the rest 16 interior IAPP peptides we constrained the corresponding beta-sheet rich regions (residues 8-17 and 28-37) and allowed rest of the unstructured loop regions to move freely.

Basic and acidic amino acids of the IAPP (fibril) were assigned charges corresponding to their titration states at physiological condition (pH=7.4) – Arg and Lys residues were assigned +1, Asp and Glu were assigned -1, while His was neutral. Counter ions (Cl⁻) were added to maintain the net charge of the systems zero and accounted for possible counter-ion condensation [47].

In simulations of EGCG binding with soluble IAPP peptides, the initial structure of the IAPP monomer was obtained from the Protein Data Bank (www.rcsb.org/pdb) with the PDB code of 2L86. We used the structure of EGCG taken from the PubChem (pubchem.ncbi.nlm.nih.gov) with the CID of 65064. The disulfide bond connecting C2 and C7 in each IAPP peptide was maintained during the DMD simulations of both soluble IAPPs and amyloid fibrils. To keep the peptide concentration fixed in the simulations of EGCG binding with various numbers of soluble IAPPs, we varied the size of a cubic simulation box with the dimension from 63.7 Å for one IAPP to 127.4 Å for eight peptides. For simulations of EGCG binding with the IAPP fibril, we used a cubic box with the dimension of 173 Å. The periodic boundary condition was used in all simulations. For data analysis, we used an inter-atomic distance cutoff of 5 Å to define an atomic contact.

Acknowledgements

This work was supported by ARC Project No. CE140100036 (Davis), NSF CAREER grant CBET-1553945 (Ding), NIH 1R35GM119691 (Ding), and an internal grant from Monash Institute of Pharmaceutical Sciences (Ke).

Electronic Supplementary Material: Supplementary material (Figs. S-1-7, Table S1) is available in the online version of this article at [http://dx.doi.org/10.1007/s12274-***-****-*](http://dx.doi.org/10.1007/s12274-***-****-) (automatically inserted by the publisher).

References

- [1] Knowles, T. P. J.; Vendruscolo, M.; Dobson, C. M. The amyloid state and its association with protein misfolding diseases. *Nat. Rev. Mol. Cell Biol.* **2014**, *15*, 384–396.
- [2] Eisenberg, D.; Jucker, M. The amyloid state of proteins in human diseases. *Cell* **2012**, *148*, 1188–1203.
- [3] Sawaya, M. R.; Sambashivan, S.; Nelson, R.; Ivanova, M. I.; Sievers, S. A.; Apostol, M. I.; Thompson, M. J.; Balbirnie, M.; Wiltzius, J. J.; McFarlane, H. T.; Madsen, A. Ø.; Riek, C.; Eisenberg, D. Atomic structures of amyloid cross-beta spines reveal varied steric zippers. *Nature* **2007**, *447*, 453–457.
- [4] Bieschke, J.; Herbst, M.; Wiglenda, T.; Friedrich, R. P.; Boeddrich, A.; Schiele, F.; Kleckers, D.; Lopez del Amo, J. M.; Grüning, B. A.; Wang, Q.; Schmidt, M. R.; Lurz, R.; Anwyl, R.; Schnoegl, S.; Fändrich, M.; Frank, R. F.; Reif, B.; Günther, S.; Walsh, D. M.; Wanker, E. E. Small-molecule conversion of toxic oligomers to nontoxic β -sheet-rich amyloid fibrils. *Nat. Chem. Biol.* **2012**, *8*, 93–101.
- [5] Bieschke, J.; Russ, J.; Friedrich, R. P.; Ehrnhoefer, D. E.; Wobst, H.; Neugebauer, K.; Wanker, E. E. EGCG remodels mature α -synuclein and amyloid- β fibrils and reduces cellular toxicity. *Proc. Natl. Acad. Sci.* **2010**, *107*, 7710–7715.
- [6] Sancini, G.; Ornaghi, F.; Balducci, C.; Forloni, G.; Gobbi, M.; Salmona, M.; Re, F. Pulmonary administration of functionalized nanoparticles significantly reduces beta-amyloid in the brain of an Alzheimer's disease murine model. *Nano Res.* **2016**, *9*, 2190–2201.
- [7] Wang, N.; He, J.; Chang, A. K.; Wang, Y.; Xu, L.; Chong, X.; Lu, X.; Sun, Y.; Xia, X.; Li, H.; Zhang, B.; Song, Y.; Kato, A.; Jones, G. W. (-)-Epigallocatechin-3-gallate inhibits fibrillogenesis of chicken cystatin. *J. Agric. Food Chem.* **2015**, *63*, 1347–1351.
- [8] Gurzov, E. N.; Wang, B.; Pilkington, E. H.; Chen, P.; Kakinen, A.; Stanley, W. J.; Litwak, S. A.; Hanssen, E. G.; Davis, T. P.; Ding, F.; Ke, P. C. Inhibition of hIAPP amyloid aggregation and pancreatic β -cell toxicity by

- OH-terminated PAMAM dendrimer. *Small* **2016**, *12*, 1615–1626.
- [9] Nedumpully-Govindan, P.; Gurzov, E. N.; Chen, P.; Pilkington, E. H.; Stanley, W. J.; Litwak, S. A.; Davis, T. P.; Ke, P. C.; Ding, F. Graphene oxide inhibits hIAPP amyloid fibrillation and toxicity in insulin-producing NIT-1 cells. *Phys. Chem. Chem. Phys.* **2016**, *18*, 94–100.
- [10] Mahmoudi, M.; Akhavan, O.; Ghavami, M.; Rezaee, F.; Ghiasi, S. M. A. Graphene oxide strongly inhibits amyloid beta fibrillation. *Nanoscale* **2012**, *4*, 7322–7325.
- [11] Li, M.; Zhao, A.; Dong, K.; Li, W.; Ren, J.; Qu, X. Chemically exfoliated WS₂ nanosheets efficiently inhibit amyloid β -peptide aggregation and can be used for photothermal treatment of Alzheimer's disease. *Nano Res.* **2015**, *8*, 3216–3227.
- [12] Nedumpully-Govindan, P.; Kakinen, A.; Pilkington, E. H.; Davis, T. P.; Ke, P. C.; Ding, F. Stabilizing off-pathway oligomers by polyphenol nanoassemblies for IAPP aggregation inhibition. *Sci. Rep.* **2016**, *6*, 19463.
- [13] Xu, C.; Shi, P.; Li, M.; Ren, J.; Qu, X. A cytotoxic amyloid oligomer self-triggered and NIR-enhanced amyloidosis therapeutic system. *Nano Res.* **2015**, *8*, 2431–2444.
- [14] Supattapone, S.; Nguyen, H. O.; Cohen, F. E.; Prusiner, S. B.; Scott, M. R. Elimination of prions by branched polyamines and implications for therapeutics. *Proc. Natl. Acad. Sci. U.S.A.* **1999**, *96*, 14529–14534.
- [15] Fischer, M.; Appelman, D.; Schwar, S.; Klajnner, B.; Bryszewski, M.; Brigitte Voi, B.; Rogers, M. Influence of surface functionality of poly(propylene imine) dendrimers on protease resistance and propagation of the scrapie prion protein. *Biomacromolecules* **2010**, *11*, 1314–1325.
- [16] Cegelski, L.; Pinkner, J. S.; Hammer, N. D.; Cusumano, C. K.; Hung, C. S.; Chorell, E.; Åberg, V.; Walker, J. N.; Seed, P. C.; Almqvist, F.; Chapman, M. R.; Hultgren, S. J. Small-molecule inhibitors target *Escherichia coli* amyloid biogenesis and biofilm formation. *Nat. Chem. Biol.* **2009**, *5*, 913–919.
- [17] Jones, O. G.; Mezzenga, R. Inhibiting, promoting, and preserving stability of functional protein fibrils. *Soft Matter* **2012**, *8*, 876–895.
- [18] Ehrnhoefer, D. E.; Bieschke, J.; Boeddrich, A.; Herbst, M.; Masino, L.; Lurz, R.; Engemann, S.; Pastore, A.; Wanker, E. E. EGCG redirects amyloidogenic polypeptides into unstructured, off-pathway oligomers. *Nat. Struct. Mol. Biol.* **2008**, *15*, 558–566.
- [19] Cao, P.; Raleigh, D. P. Analysis of the inhibition and remodeling of islet amyloid polypeptide amyloid fibers by flavanols. *Biochemistry* **2012**, *51*, 2670–2683.
- [20] Meng, F.; Abedini, A.; Plesner, A.; Verchere, C. B.; Raleigh, D. P. The flavanol (-)-epigallocatechin 3-gallate inhibits amyloid formation by islet amyloid polypeptide, disaggregates amyloid fibrils, and protects cultured cells against IAPP-induced toxicity. *Biochemistry* **2010**, *49*, 8127–8133.
- [21] Palhano, F. L.; Lee, J.; Grimster, N. P.; Kelly, J. W. Toward the molecular mechanism(s) by which EGCG treatment remodels mature amyloid fibrils. *J. Am. Chem. Soc.* **2013**, *135*, 7503–7510.
- [22] Engel, M. F. M.; vandenAkker, C. C.; Michael Schleegeer, M.; Velikov, K. P.; Koenderink, G. H.; Bonn, M. The polyphenol EGCG inhibits amyloid formation less efficiently at phospholipid interfaces than in bulk solution. *J. Am. Chem. Soc.* **2012**, *134*, 14781–14788.
- [23] vandenAkker, C. C.; Deckert-Gaudig, T.; Schleegeer, M.; Velikov, K. P.; Deckert, V.; Bonn, M.; Koenderink, G. H. Nanoscale heterogeneity of the molecular structure of individual hIAPP amyloid fibrils revealed with tip-enhanced Raman spectroscopy. *Small* **2015**, *11*, 4131–4139.
- [24] Lara, C.; Gourdin-Bertin, S.; Adamcik, J.; Bolisetty, S.; Mezzenga, R. Self-assembly of ovalbumin into amyloid and non-amyloid fibrils. *Biomacromolecules* **2012**, *13*, 4213–4221.
- [25] Granqvist, C. G.; Buhrman, R. A. Ultrafine metal particles. *J. Appl. Phys.* **1976**, *47*, 2200–2219.
- [26] Usov, I.; Adamcik, J.; Mezzenga, R. Polymorphism in bovine serum albumin fibrils: morphology and statistical analysis. *Faraday Discuss.* **2013**, *166*, 151–162.
- [27] Usov, I.; Mezzenga, R. FiberApp: an open-source software for tracking and analyzing polymers, filaments, biomacromolecules, and fibrous objects. *Macromolecules* **2015**, *48*, 1269–1280.
- [28] Adamcik, J.; Jung, J. M.; Flakowski, J.; De Los Rios, P.; Dietler, G.; Mezzenga, R. Understanding amyloid aggregation by statistical analysis of atomic force microscopy images. *Nat. Nanotechnol.* **2010**, *5*, 423–428.
- [29] Bolisetty, S.; Adamcik, J.; Mezzenga, R. Snapshots of fibrillation and aggregation kinetics in multistranded amyloid β -lactoglobulin fibrils. *Soft Matter* **2011**, *7*, 493–499.
- [30] Lara, C.; Adamcik, J.; Jordens, S.; Mezzenga, R. General self-assembly mechanism converting hydrolyzed globular proteins into giant multistranded amyloid ribbons. *Biomacromolecules* **2011**, *12*, 1868–1875.
- [31] Jeong, J. S.; Ansaloni, A.; Mezzenga, R.; Lashuel, H. A.; Dietler, G. Novel mechanistic insight into the molecular basis of amyloid polymorphism and secondary nucleation during amyloid formation. *J. Mol. Biol.* **2013**, *425*, 1765–1781.
- [32] Tycko, R. Molecular structure of amyloid fibrils: insights from solid-state NMR. *Q. Rev. Biophys.* **2006**, *39*, 1–55.
- [33] Luca, S.; Yau, W. M.; Leapman, R.; Tycko, R. Peptide conformation and supramolecular organization in amylin fibrils: constraints from solid-state NMR. *Biochemistry* **2007**, *46*, 13505–13522.
- [34] Reches, M.; Gazit, E. Casting metal nanowires within discrete self-assembled peptide nanotubes. *Science* **2003**,

- 300, 625–627.
- [35] Knowles, T. P. J.; Waudby, C. A.; Devlin, G. L.; Cohen, S. I. C.; Aguzzi, A.; Vendruscolo, M.; Terentjev, E. M.; Welland, M. E.; Dobson, C. M. An analytical solution to the kinetics of breakable filament assembly. *Science* **2009**, *326*, 1533–1537.
- [36] Sang, S.; Lee, M.-J.; Hou, Z.; Ho, C.T.; Yang, C. S. Stability of tea polyphenol (-)-epigallocatechin-3-gallate and formation of dimers and epimers under common experimental conditions. *J. Agric. Food Chem.* **2005**, *53*, 9478-9484.
- [37] Knowles, T. P. J.; Buehler, M. J. Nanomechanics of functional and pathological amyloid materials. *Nat. Nanotechnol.* **2011**, *6*, 469–479.
- [38] Allen, M. P., Tildesley, D. J. *Computer simulation of liquids*; Clarendon Press: Oxford, 1989.
- [39] Rapaport, D. C. *The art of molecular dynamics simulation*. Bar-Ilan University: Israel, 2004.
- [40] Ding, F.; Dokholyan, N. V. Emergence of protein fold families through rational design. *PLoS Comput. Biol.* **2006**, *2*, e85.
- [41] Yin, S.; Biedermannova, L.; Vondrasek, J.; Dokholyan, N. V. MedusaScore: An accurate force field-based scoring function for virtual drug screening. *J. Chem. Inf. Model.* **2008**, *48*, 1656–1662.
- [42] Neria, E.; Fischer, S.; Karplus, M. Simulation of activation free energies in molecular systems. *J. Chem. Phys.* **1996**, *105*, 1902–1921.
- [43] Lazaridis, T.; Karplus, M. Effective energy functions for protein structure prediction. *Curr. Opin. Struct. Biol.* **2000**, *10*, 139–145.
- [44] Andersen, H. C. Molecular dynamics simulations at constant pressure and/or temperature. *J. Chem. Phys.* **1980**, *72*, 2384–2393.
- [45] Ding, F.; Dokholyan, N. V. Incorporating backbone flexibility in MedusaDock improves ligand-binding pose prediction in the CSAR2011 docking benchmark. *J. Chem. Inf. Model.* **2013**, *53*, 1871–1879.
- [46] Nedumpully-Govindan, P.; Jemec, D. B.; Ding, F. CSAR benchmark of flexible MedusaDock in affinity prediction and nativelike binding pose selection. *J. Chem. Inf. Model.* **2016**, *56*, 1042-1052.
- [47] Manning, G. S. Limiting Laws and counterion condensation in polyelectrolyte solutions I. colligative properties. *J. Chem. Phys.* **1969** *51*, 924–933.

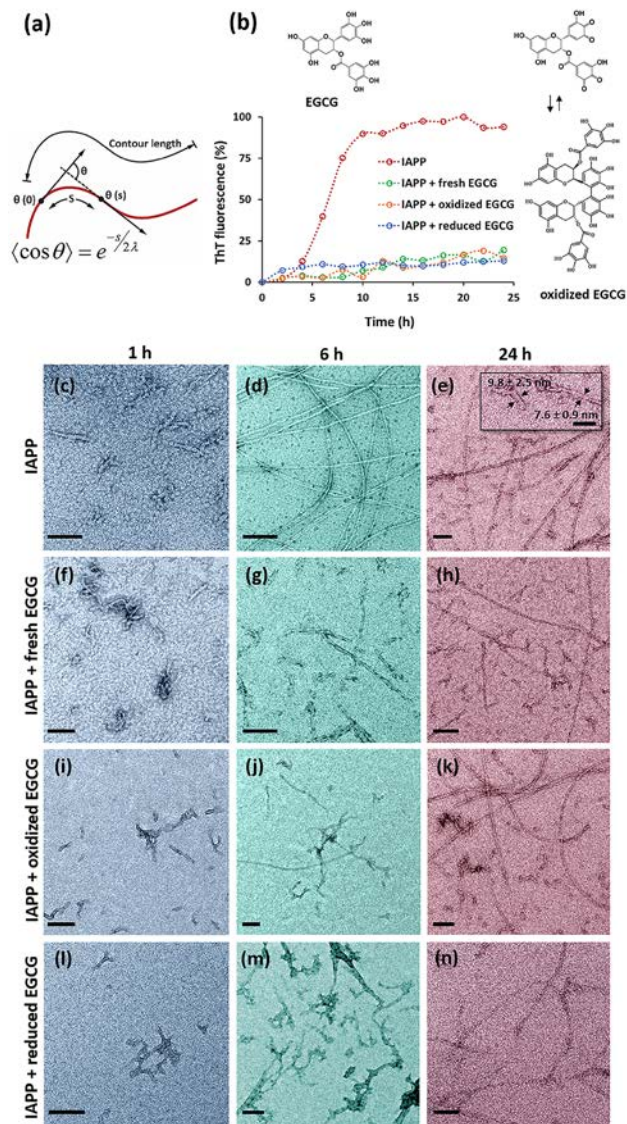


Figure 1. (a) Schematic definitions of contour length and persistence length (λ) of a fibril. The persistence length λ is defined as the length over which angular correlations in the tangent direction decrease by e times. The factor 2 in the formula accounts for the 2D Euclidean Geometry. (b) ThT kinetic experiment of IAPP fibrillation in the presence of fresh EGCG, oxidized EGCG and reduced EGCG. (c-n) TEM images of IAPP fibrillization at 1 h (c, f, i, l), 6 h (d, g, j, m) and 24 h (e, h, k, n) of incubation time with/without EGCG species. (c-e) IAPP alone. (f-h) IAPP incubated with fresh EGCG. (i-k) IAPP incubated with oxidized EGCG. (l-n) IAPP incubated with GSH-reduced EGCG. All chemicals were prepared at $50 \mu\text{M}$ in concentration and mixed with a 1:1 molar ratio where apply. Scale bar: 100 nm.

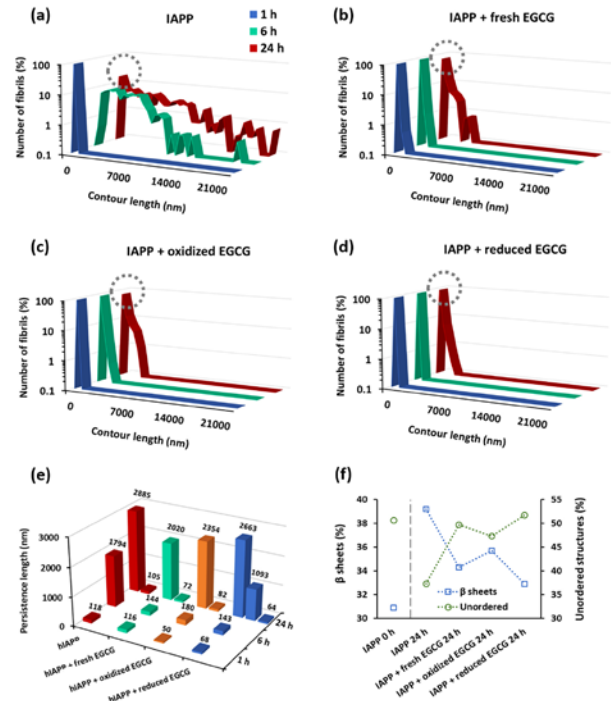


Figure 2. Contour length of IAPP fibrils incubated for 0-24 h for IAPP control (a) and IAPP incubated with fresh, oxidized and reduced EGCG (b-d). The dashed yellow circle corresponds to a population of small protofibrils at 24 h. The dashed grey circles indicate populations of small fibrils at 24 h (b-d). (e) IAPP fibril persistence length versus time for the four sample conditions. (f) Secondary structures of IAPP incubated with fresh EGCG, oxidized EGCG and reduced EGCG after 24 h of incubation, showing reduced β -sheets and increased unordered content compared with the IAPP control. All chemicals were prepared at $50 \mu\text{M}$ in concentration and mixed with a 1:1 molar ratio where apply.

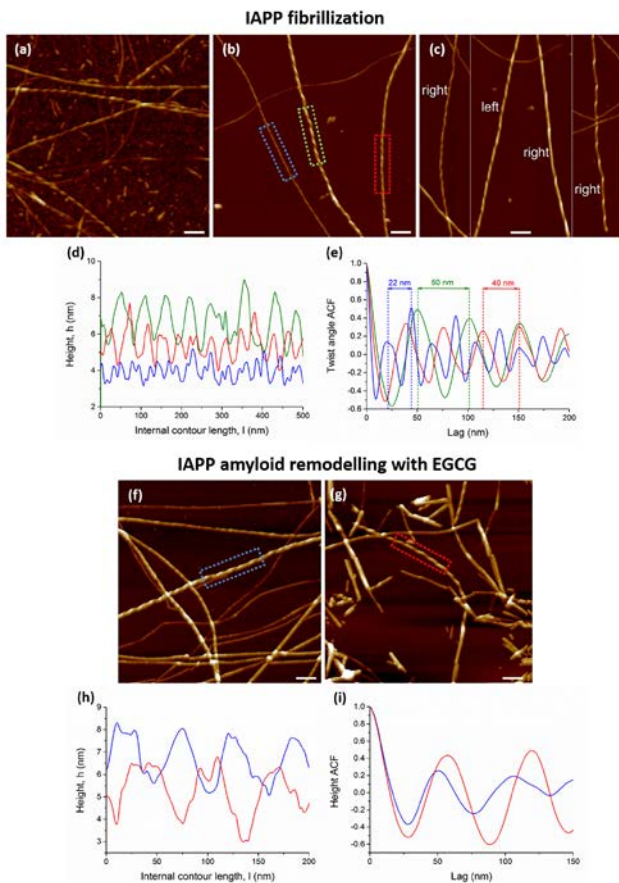


Figure 3. Effect of fibrillization time on the morphology and periodicity of IAPP fibrils (50 μ M). (a) 3D AFM image of IAPP fibrils at 6 h of incubation. (b) 3D AFM image of IAPP fibrils at 24 h of incubation. (c) 3D AFM images of left- and right-handed IAPP fibrils at 24 h of incubation. (d) The height profiles along the IAPP fibrils displayed in panel b. (e) Estimation of the periodicities of IAPP fibrils displayed in panel b by twist angle autocorrelation function. (f-i) Remodelling of mature IAPP amyloids with EGCG (oxidized form) (Both components of 50 μ M). (f) 3D AFM image of 1 month old IAPP amyloids. (g) EGCG remodelled 1 month old IAPP amyloids (24 h incubation at 20 $^{\circ}$ C), resulting in sharply truncated and kinked IAPP fibrils. (H) Height profiles of IAPP fibrils without (blue line) and with EGCG (red line). (i) Pitch size estimation of IAPP fibrils without (blue line) and with EGCG (red line) based on height autocorrelation function. Scale bars: 100 nm.

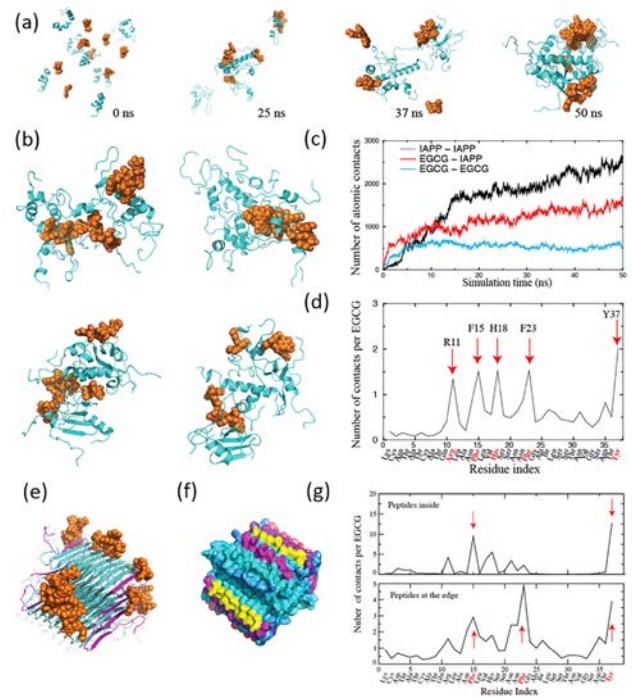


Figure 4. (a-d) DMD simulations of eight EGCG ligands binding with eight IAPPs. (a) Snapshot structures illustrate the aggregation process. IAPP: cyan. EGCG: orange. (b) Final aggregate structures from four independent simulations. (c) Trajectories of the total number of atomic contacts between IAPP-IAPP (black), EGCG-IAPP (red), and EGCG-EGCG (cyan), averaged over ten independent simulations. (d) Number of atomic contacts between EGCG and individual residues in IAPP, averaged by the number of both peptides and ligands. The residues bound strongly with EGCG are indicated by arrows. (e-g) DMD simulations of EGCG remodelling IAPP fibrils (Model 1). (e) Twenty EGCG binding with two layers of IAPP decamer protofibrils stacked together. The peptides at the edges (magenta) and inside the fibril (cyan) are shown in cartoon representation. EGCG molecules (orange) are illustrated in spherical representation. The peptides at the edges were free to move during simulations. (f) Surface structure of the IAPP fibril with EGCG binding of low, intermediate and high (cyan, magenta and yellow) binding frequencies. (g) Number of atomic contacts between EGCG and individual IAPP residues, averaged over the numbers of EGCG and IAPP. The upper panel represents binding with the peptides inside the fibrillar structure and the lower panel corresponds to binding with four IAPP peptides at the edges.

Electronic Supplementary Material

Nanoscale inhibition of polymorphic and ambidextrous IAPP amyloid aggregation with small molecules

Aleksandr Kakinen,¹ Jozef Adamcik,² Bo Wang,³ Xinwei Ge,³ Raffaele Mezzenga,²(✉) Thomas P. Davis,^{1,4}(✉) Feng Ding,³(✉) and Pu Chun Ke¹(✉)

¹ARC Centre of Excellence in Convergent Bio-Nano Science and Technology, Monash Institute of Pharmaceutical Sciences, Monash University, 381 Royal Parade, Parkville, VIC 3052, Australia

²Food & Soft Materials, Department of Health Science & Technology, ETH Zurich, Schmelzbergstrasse 9, LFO, E23, 8092 Zurich, Switzerland

³Department of Physics and Astronomy, Clemson University, Clemson, SC 29634, USA

⁴Department of Chemistry, Warwick University, Gibbet Hill, Coventry, CV4 7AL, United Kingdom

Supporting information to DOI 10.1007/s12274-****-****-* (automatically inserted by the publisher)

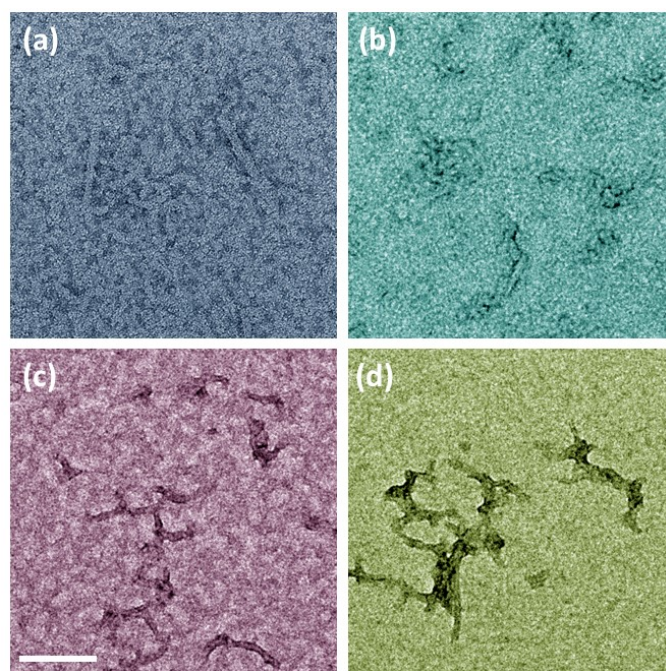


Figure S-1. TEM imaging of IAPP incubation with EGCG for 20 min. (a) IAPP alone. (b) IAPP + fresh EGCG. (c) IAPP + oxidized EGCG. (d) IAPP + reduced EGCG. Scale bar: 100 nm. The molar ratio of EGCG/IAPP was kept at 1:1 for all

mixtures.

Address correspondence to Raffaele Mezzenga, raffaele.mezzenga@hest.ethz.ch; Thomas P. Davis, thomas.p.davis@monash.edu; Feng Ding, fding@clemson.edu; and Pu Chun Ke, pu-chun.ke@monash.edu

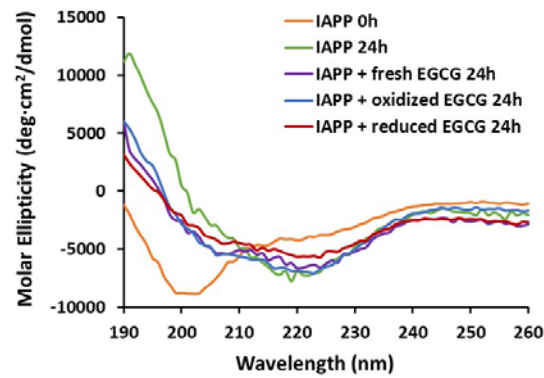


Figure S-2. Circular dichroism (CD) spectra of IAPP at 0 h and 24 h, and IAPP with fresh EGCG, oxidized EGCG and reduced EGCG after 24 h of incubation (control spectra subtracted).

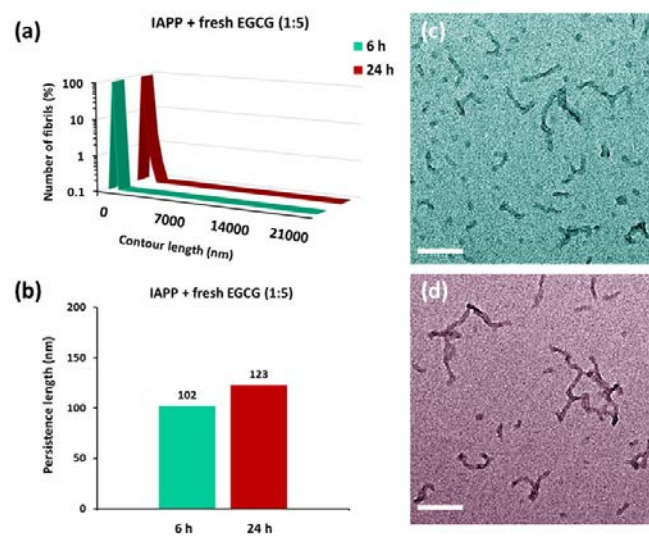


Figure S-3. Physical properties of IAPP fibrillization in the presence of fresh EGCG at 6 h and 24 h of incubation. (a) Contour length distributions of IAPP-EGCG at 6 h and 24 h of incubation. (b) Persistence lengths of IAPP-EGCG at 6 h and 24 h of incubation. (c) TEM image of IAPP-EGCG at 6 h of incubation. (d) TEM image of IAPP-EGCG at 24 h of incubation. Scale bars: 100 nm.

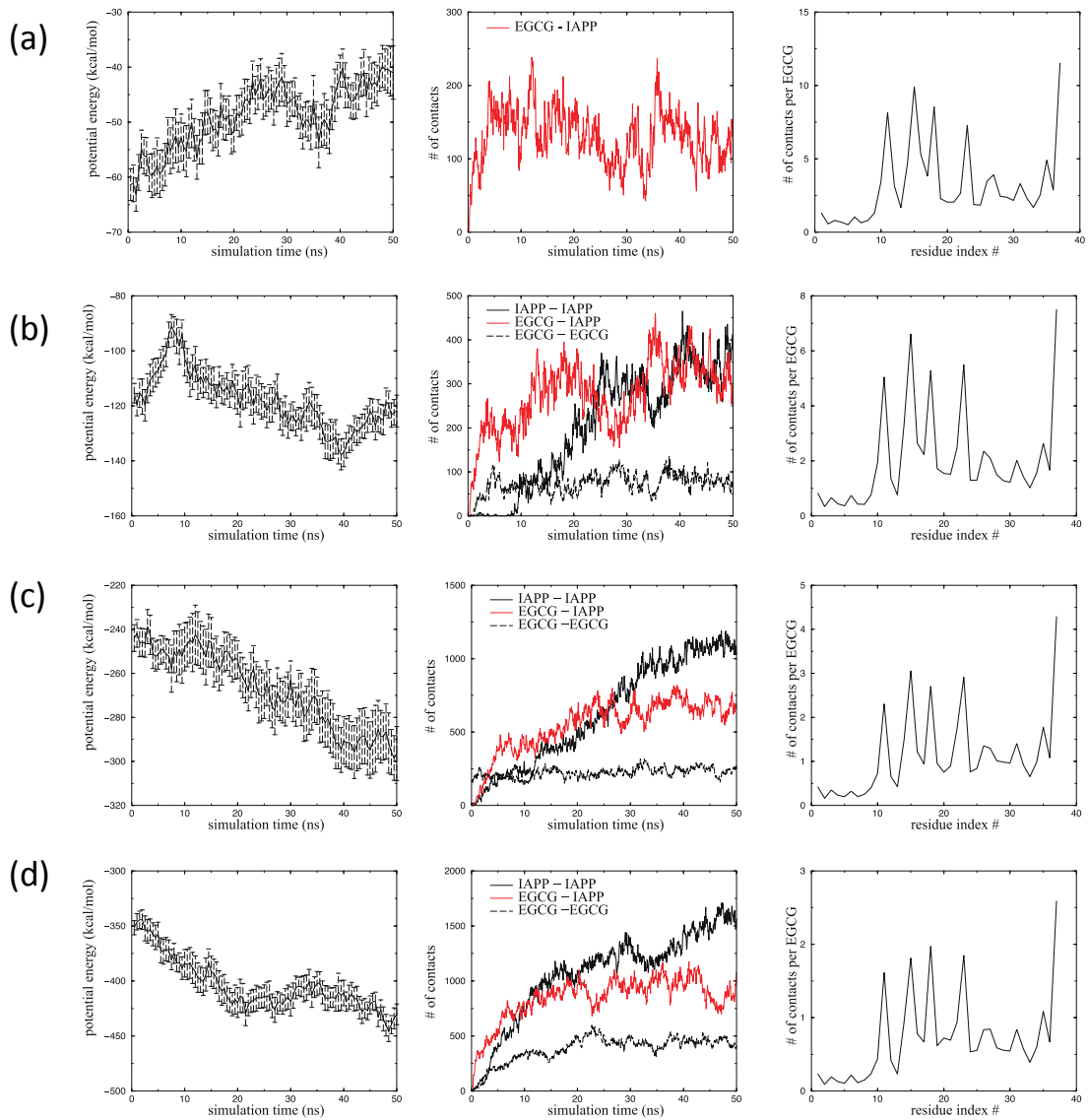


Figure S-4. DMD simulations with various numbers of EGCGs and IAPPs: (a) 1:1, (b) 2:2, (c) 4:4 and (d) 6:6. All data were averaged from 10 independent simulations for each molecular system. The trajectories of potential energy with error bars are illustrated on the left. Plots in the middle demonstrate the trajectories of total number of contacts among IAPPs (black solid line), between EGCG and IAPP (red solid line), and among EGCGs (dash line). The plots on the right show the binding frequency of per EGCG to different IAPP residues.

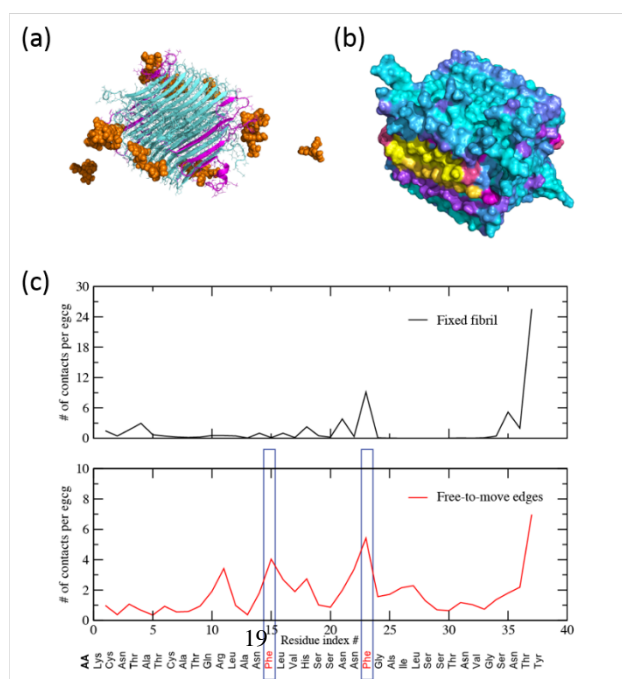


Figure S-5. DMD simulation of EGCG remodelling IAPP fibrils (Model 2). (a) A snapshot structure from DMD simulations. (b) Binding sites of EGCG on IAPP fibril. (c) The average number of atomic contacts between EGCG and individual IAPP residues. The upper panel represents binding to interior peptides and the lower panel corresponds to binding to edge peptides. The same labels and colour schemes as in Figs. 4e, f are used here.

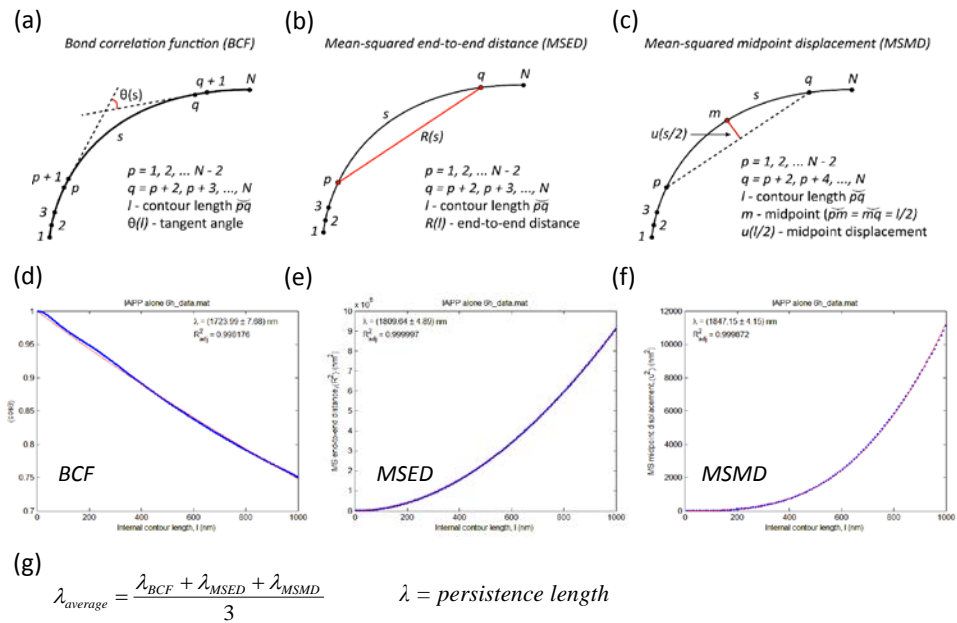


Figure S-7. DMD simulations of IAPP aggregation and remodelling of IAPP fibrils with Theasinensin A (ThA), a cross-linked EGCG dimer. (a) Trajectories of the total number of contact among different species, averaged from 10 independent simulations. (b) Number of atomic contacts between ThA and individual IAPP residues, averaged over the numbers of both ThA and IAPP. The binding sites are indicated in red for the peptide residues. (c) Snapshot structures illustrating IAPP (cyan) aggregation in the presence of ThA (orange), with a ThA/IAPP ratio of 3:6. (d) Binding of ten ThAs with two layers of IAPP decamer protofibrils stacked together (Model 1). The peptides at the edges are shown in magenta while the rest in cyan. (e) Number of atomic contacts between ThA and individual IAPP residues, averaged over the numbers of ThA and IAPP. The upper panel represents binding with the peptides inside the fibrillar structure and the lower panel corresponds to binding with four IAPP peptides at the edges.

Table S1. Number of fibrils analyzed per sample condition.

Time	Number of fibrils analyzed				
	hIAPP	IAPP + fresh EGCG	IAPP + oxidized EGCG	IAPP + reduced EGCG	IAPP + fresh EGCG (1:5)
1 h	160	188	183	171	-
6 h	201	220	218	175	254
24 h	559	443	420	534	318